Mass-shedding Activities of Asteroid (3200) Phaethon Enhanced by Its Rotation

Ryota Nakano and Masatoshi Hirabayashi
Department of Aerospace Engineering Auburn University, 211 Davis Hall, Auburn, AL 36849, USA; rzn0040@auburn.edu

Abstract

Asteroid (3200) Phaethon, a B-type asteroid, has been active during its perihelion passages. This asteroid is considered to be a source of the Geminid meteor stream. It is reported that this asteroid is spinning at a rotation period of 3.60 hr and has a top shape (an oblate body with an equatorial ridge) with a mean equatorial diameter of 6.25 km. Here, we report that Phaethon's rotation state may be close to or above its critical rotation period when the bulk density is 0.5–1.5 g cm^{-3} (a typical bulk density of a B-type asteroid). We found that in this condition, the structure of Phaethon is sensitive to failure unless the cohesive strength is $\sim 50 - \sim 260$ Pa. This result implies that if there are some surface processes driven by, for example, thermal waves, large-scaled deformation may happen and cause mass shedding. From this interpretation, we propose the processes that produced the Geminid meteor stream in the past and dust tails recently. Phaethon initially rotated at a spin period shorter than the current period. The magnitude of structural deformation at this stage was higher than the present spin condition, and a large mass-shedding event, i.e., the Geminid meteor stream, occurred. After this deformation process, the body became more oblate, and its spin slowed down. At this point, while the spin was high enough for the body to have mass-shedding events, the magnitude of these events became small.

Unified Astronomy Thesaurus concepts: Near-Earth objects (1092); Asteroids (72); Planetary structure (1256); Planetary science (1255); Planetary surfaces (2113); Meteor streams (1035); Meteors (1041)

1. Introduction

Asteroid (3200) Phaethon may be a source of the Geminid meteor stream (Whipple 1983; Gustafson 1989; Williams & Wu 1993) and has been observed for a long time (Cochran & Barker 1984; Chamberlin et al. 1996; Hsieh & Jewitt 2005; Wiegert et al. 2008). In 2009 (Jewitt & Li 2010) and 2012 (Li & Jewitt 2013), dust tails from Phaethon were observed during the perihelion passage, revealing that this asteroid is indeed an active asteroid. However, the activities detected near the perihelion left a mystery of the production of the Geminid meteor stream. The dust mass inferred from the observations is $\sim 3 \times 10^5$ kg (Li & Jewitt 2013), which is much smaller than the estimated mass of the Geminid meteor stream, 10^{12}–10^{13} kg (Hughes & McBride 1989; Jenniskens 1994). Also, the estimated average mass-loss rate of 3 kg s^{-1} is too small to replenish the Geminid meteor stream mass (Jewitt et al. 2013), if the dynamical lifetime of the Geminid meteor stream is $\sim 10^3$ yr (Gustafson 1989; Ryabova 2007). While most of the proposed mechanisms were found incapable of producing dust tails, thermal fracture and cracking due to dehydration in surface materials might be reasonable processes to generate dust tails (Jewitt & Li 2010; Jewitt 2012; Li & Jewitt 2013).

Radar observations during the 2017 apparition revealed Phaethon's shape. Taylor et al. (2019) reported that Phaethon might be an oblate shape with an equatorial ridge, or the so-called top shape. The equivalent diameter of this asteroid was estimated to be 6 km. The examples of top-shaped asteroids are OSIRIS-REx's target (101955) Bennu (Lauretta et al. 2019) and Hayabusa2's target (162173) Ryugu (Kitazato et al. 2019; Sugita et al. 2019; Watanabe et al. 2019). Phaethon is currently spinning at a rotation period of 3.60 hr (Taylor et al. 2019). The radar albedo is reported to be the lowest among the cataloged near-Earth asteroids (Taylor et al. 2019), implying that its spectral type is consistent with a B type (Taylor et al. 2019),

and thus the bulk density may be as low as ~ 1.0 g cm^{-3} (Scheeres et al. 2019; Watanabe et al. 2019).

We hypothesize that the mass-shedding activities of Phaethon may have been enhanced by fast rotation, given recent work arguing that the equatorial ridges of top-shaped asteroids were evolved by rotationally driven reshaping (Walsh et al. 2008, 2012). We propose that structural failure on the surface and/or inside the body triggered by fast rotation plays an important role in the mass-shedding mechanism. This study provides better insights into the physical activities of Phaethon to support DESTINY+, a planned flyby mission concept led by the Japan Aerospace Exploration Agency (Arai et al. 2018).

2. Semi-analytical Model for Structural Failure in a Top-shaped Body

Phaethon was reported to be a top-shaped body. Recent work has shown that the global failure condition in uniformly rotating top shapes can be roughly determined by assuming that they are triaxial ellipsoids (Hirabayashi 2015). For Phaethon, the shape is not well known at present while an effort in analyzing it from radar observation data is being made (P. A. Taylor 2020, personal communication). Therefore, a simplified model that uses a triaxial ellipsoid can still reasonably provide structural failure in this asteroid. We note that the heterogeneity in structural failure may be critical once the detailed shape of this asteroid is considered (Hirabayashi & Scheeres 2019).

We consider that Phaethon has a mean equatorial diameter of 6.25 km and an oblateness (the ratio of semiminor axis to semimajor axis) of 0.889, which is the same as Bennu's (Barnouin et al. 2019). We note that Taylor et al. (2019) did not specify the oblateness of Phaethon but implied that it would be similar than that of Bennu. For the oblateness, we do not account for the semi-intermediate axis to simplify the discussion. We assume that Phaethon's structure is uniform because the internal condition is unknown. We consider three

types of the bulk density, 0.5, 1.0, and 1.5 g cm^{-3}, the average of which is consistent with that of a B-type asteroid (Scheeres et al. 2019). Later, we denote the oblateness, the bulk density, and the gravitational constant as ϵ, ρ, and G, respectively. Phaethon is assumed to be rotating along the maximum principal axis. We define a three-dimensional Cartesian coordinate system such that the z-axis is lined up along the rotation axis, and the x- and y-axes are along the maximum and intermediate moment of inertia axes, respectively, on the equatorial plane. Using these definitions, we compute how Phaethon experiences structural failure at a give rotation period, P.

To determine the failure condition of Phaethon, we extend the technique by Hirabayashi (2015), who only considered a sphere. We analyze when the stress field in a given element reaches its yield condition. In this model, the material behavior is assumed to be elastic-perfectly plastic, where a plastic flow begins once the stress reaches its yield condition without material hardening and softening. To describe such a material behavior, we use the following material properties: Poisson's ratio, ν; Young's modulus, E; the angle of friction, ϕ; and the cohesive strength, Y. It is worth noting that the evolution of plastic deformation is a function of loading paths. However, our purpose is not to track plastic deformation but to determine what element would first have its plastic state in a quasi-static condition where deformation is small enough that the time variation is negligible (Hirabayashi 2015).

Although we follow the terminologies of the cohesive strength by Hirabayashi (2015), we reintroduce them here to facilitate the following discussion. We compute the minimum cohesive strength that can prevent structural failure of a given element in an asteroid rotating at P. We call this strength "critical cohesive strength" and denote it as Y^*. On the other hand, we use "actual cohesive strength" as an assumed strength that an asteroid may have. We denote this as Y. Also, the critical rotation period P_c is the rotation period at which a small particle on the equatorial surface of Phaethon gains the centrifugal acceleration larger than the gravitational acceleration and is lifted off from the surface.

2.1. Stress Field Computation

Similar to Hirabayashi et al. (2015) and Hirabayashi (2015), we apply a technique by Dobrovolskis (1982) and Holsapple (2001) to provide an elastic stress in a triaxial ellipsoid that is uniformly spinning at a rotation period of P. Here, while noting that the details are found in Dobrovolskis (1982), we briefly introduce the formulation process. The displacement u in Cartesian coordinates can be expressed in terms of 12 unknown constants A through L:

$$u_x = x\left[A + B\frac{x^2}{a^2} + C\frac{y^2}{b^2} + D\frac{z^2}{c^2}\right], \tag{1}$$

$$u_y = y\left[E + F\frac{x^2}{a^2} + G\frac{y^2}{b^2} + H\frac{z^2}{c^2}\right], \tag{2}$$

$$u_z = z\left[I + J\frac{x^2}{a^2} + K\frac{y^2}{b^2} + L\frac{z^2}{c^2}\right], \tag{3}$$

where a, b, and c ($a \geqslant b \geqslant c$) are the principle semi-axes of the triaxial ellipsoid. The strain is obtained by

$$\epsilon_{ij} = \frac{1}{2}\left(\frac{\partial u_i}{\partial x_j} + \frac{\partial u_j}{\partial x_i}\right). \tag{4}$$

Applying Hooke's law, the stress tensor is also expressed in terms of A through L:

$$\sigma_{ij} = \lambda\epsilon_{kk}\delta_{ij} + 2\mu\epsilon_{ij}, \tag{5}$$

where $\epsilon_{kk} = \epsilon_{xx} + \epsilon_{yy} + \epsilon_{zz}$, and δ_{ij} is the Kronecker delta. λ and μ are the Lame's constants obtained from

$$\lambda = \frac{E\nu}{(1+\nu)(1-2\nu)}, \tag{6}$$

$$\mu = \frac{E}{2(1+\nu)}. \tag{7}$$

To determine the 12 unknown constants, we must impose 12 linearly independent relations. The stresses σ_{ij} in a body in equilibrium under body forces must satisfy the stress equilibrium equations:

$$\frac{\partial}{\partial x_j}\sigma_{ji} = -\rho b_i, \tag{8}$$

where b_i is the body force, which is driven by gravitational and rotational effects in our problem. Equation (8) provides three constraints out of the 12 required relations. The remaining nine relations are then imposed from the traction free boundary condition:

$$\sigma_{ij}n_j = 0, \tag{9}$$

where n_j is the unit normal to the surface and given by

$$n_x = \frac{x}{a^2 w}, \tag{10}$$

$$n_y = \frac{y}{b^2 w}, \tag{11}$$

$$n_z = \frac{z}{c^2 w}, \tag{12}$$

where

$$w = \left(\frac{x^2}{a^4} + \frac{y^2}{b^4} + \frac{z^2}{c^4}\right)^{1/2}. \tag{13}$$

The 12 unknown constants are, hence, provided by 12 linearly independent relations.

2.2. Structural Failure Condition

Once the stress field is obtained from the previous section, we use it to determine the structural failure condition of a given element. Here, we apply the Drucker–Prager yield criterion, a smooth approximation of the Mohr–Coulomb yield criterion (Chen & Han 1988):

$$f = \alpha I_1 + \sqrt{J_2} - s \leqslant 0. \tag{14}$$

I_1 and J_2 are the stress invariants:

$$I_1 = \sigma_1 + \sigma_2 + \sigma_3, \tag{15}$$

$$J_2 = \frac{1}{6}\{(\sigma_1 - \sigma_2)^2 + (\sigma_2 - \sigma_3)^2 + (\sigma_3 - \sigma_1)^2\}, \tag{16}$$

Table 1
Parameter Settings

Parameter	Symbol	Value	Units
Gravitational constant	G	6.6738×10^{-11}	$\mathrm{m^3 \cdot kg^{-1} \cdot s^{-2}}$
Semimajor axis	a	3200	m
Semiminor axis	c	2847	m
Oblateness	ϵ	0.889	...
Current rotation period	P	3.60	hr
Bulk density	ρ	0.5, 1.0, 1.5	$\mathrm{g \cdot cm^{-3}}$
Poisson's ratio	ν	0.25	...
Elastic modulus	E	10^7	Pa
Friction angle	ϕ	35	deg

where σ_i ($i = 1, 2, 3$) is the principal stress component, which can be obtained from the derived stress field above. α and s are material constants and given by (Chen & Han 1988)

$$\alpha = \frac{2 \sin \phi}{\sqrt{3} \, (3 - \sin \phi)}, \tag{17}$$

$$s = \frac{6Y \cos \phi}{\sqrt{3} \, (3 - \sin \phi)}. \tag{18}$$

From the equal condition of Equation (14), we obtain the following expression for Y^*:

$$Y^* = \frac{\sqrt{3} \, (3 - \sin \phi)}{6 \cos \phi} (\alpha I_1 + \sqrt{J_2}). \tag{19}$$

If Equation (19) becomes negative, we consider Y^* to be 0 Pa, which means that no strength is necessary for an element to keep the original shape.

3. Results

We investigate the critical cohesive strength based on the following assumed parameters, $\nu = 0.25$, $E = 10^7$ Pa, and $\phi = 35°$, to make our discussion consistent with earlier work (e.g., Hirabayashi & Scheeres 2015). We note that Young's modulus does not influence our stress field calculation (Love 2013), and the variations in Poisson's ratio and the angle of friction do not affect our results for geological materials significantly (Lambe & Whitman 1969; Hirabayashi & Scheeres 2019). The current rotation period is set to be 3.60 hr (Taylor et al. 2019). We consider the bulk density to be 0.5, 1.0, and 1.5 g cm^{-3}. Table 1 lists the parameters considered in the current study.

We find that the failure mode varies with the bulk density. We plot the distribution of Y^* at the x–z plane for different densities in Figure 1. Panels (a), (b), and (c) describe the bulk densities of 0.5, 1.0, and 1.5 g cm^{-3}, respectively. In this range of the bulk density, the body should have a cohesive strength to keep the original shape. For the case of $\rho = 0.5$ g cm^{-3}, P_c is found to be 4.83 hr. Therefore, the current rotation period is shorter than P_c, indicating that materials should be shed and highly sensitive to structural failure. Figure 1(a) shows $Y^* > 0$ everywhere except the pole region. Y^* is higher in the interior than on the surface, and its maximum value is 259 Pa at the center. This indicates that the interior is more sensitive to structural failure than the surface. If the actual cohesive strength Y is smaller than Y^*, the central region structurally fails first. For the case of $\rho = 1.0$ g cm^{-3}, P_c is found to be 3.42 hr and is shorter than the current period. However, the interior still

exhibits high Y^* in the major regions (panel (b)). The maximum value of Y^* is 179 Pa and is located at the center. For the case of $\rho = 1.5$ g cm^{-3}, P_c is found to be 2.79 hr. Unlike the other two cases, the interior has $Y^* = 0$ in the most areas; however, high Y^* is still distributed beneath the surface ($\sim$50 Pa; panel (c)).

All three of these cases show the sensitivity of Phaethon to structural failure. This body needs a cohesive strength to keep the original condition without shape deformation. However, if there is a trigger of reshaping, it is likely that the deformation process would be enhanced by rotation, as seen from the derived sensitivity. Because of the observed activities, the cohesive strength of Phaethon is $\sim$50 – $\sim$260 Pa, depending on the bulk density. This range is consistent with that of observed small bodies (Scheeres & Sánchez 2018).

4. Discussions

Generation of dust tails at present. During perihelion passage in 2009 and 2012, the observations of Phaethon's dust tails revealed that this asteroid was an active asteroid (Jewitt & Li 2010; Li & Jewitt 2013). While the detailed mechanisms are not well known, thermal waves may be one of the plausible explanations for the reported mass-shedding activities (Li & Jewitt 2013).

At the current rotation period of 3.60 hr, the body is sensitive to structural failure regardless of the bulk density and thus needs cohesive strength to maintain its shape. The derived cohesive strength of Phaethon is less than $\sim$50 – $\sim$260 Pa, which is consistent with that of small bodies ranging up to a few hundred pascals (Scheeres & Sánchez 2018). We interpret this sensitivity as a potential enhancement of mass shedding. If there is a trigger of reshaping even at small scales, the structure of Phaethon would be perturbed, leading to rotationally driven reshaping at larger scales. Such a trigger can be thermal waves in thin surface layers (Jewitt & Li 2010; Jewitt 2012; Li & Jewitt 2013). Micrometeoroid impacts or other processes may also be possible, as seen on Bennu (Lauretta et al. 2019), although thermal waves, again, are more consistent to explain the activities of Phaethon around its perihelion passage (Li & Jewitt 2013).

Possible source of the Geminid meteor stream. We expect that rotationally induced structural failure makes Phaethon more oblate, i.e., ϵ becomes lower (Hirabayashi 2015). Because the angular momentum is constant during deformation, Phaethon may have been less oblate and rotated faster at an earlier stage before it had large deformation. Figure 2 shows the dependence of P on ϵ and P_c for different bulk densities. We find that if Phaethon is less oblate, the rotation period is shorter, and thus Y^* should be higher at a shorter rotation period. If Phaethon is a sphere ($\epsilon = 1.0$; $a = b = c$), which is the shape condition that is the least affected by rotation, the rotation period should become $P = 3.38$ hr. Figure 3 shows the distribution of Y^* for this case. Similar features observed in Figure 1 are evident in this case; however, Y^* is higher, implying that Phaethon should have been more sensitive to structural failure at a shorter rotation period. Therefore, the failure mode may become severer, and more materials should be shed significantly at a shorter rotation period.

From these results, we propose a possible evolution scenario of Phaethon (Figure 4). Phaethon was originally less oblate and spinning at a shorter rotation period than the current period. This stage is before the Geminid meteor stream was generated.
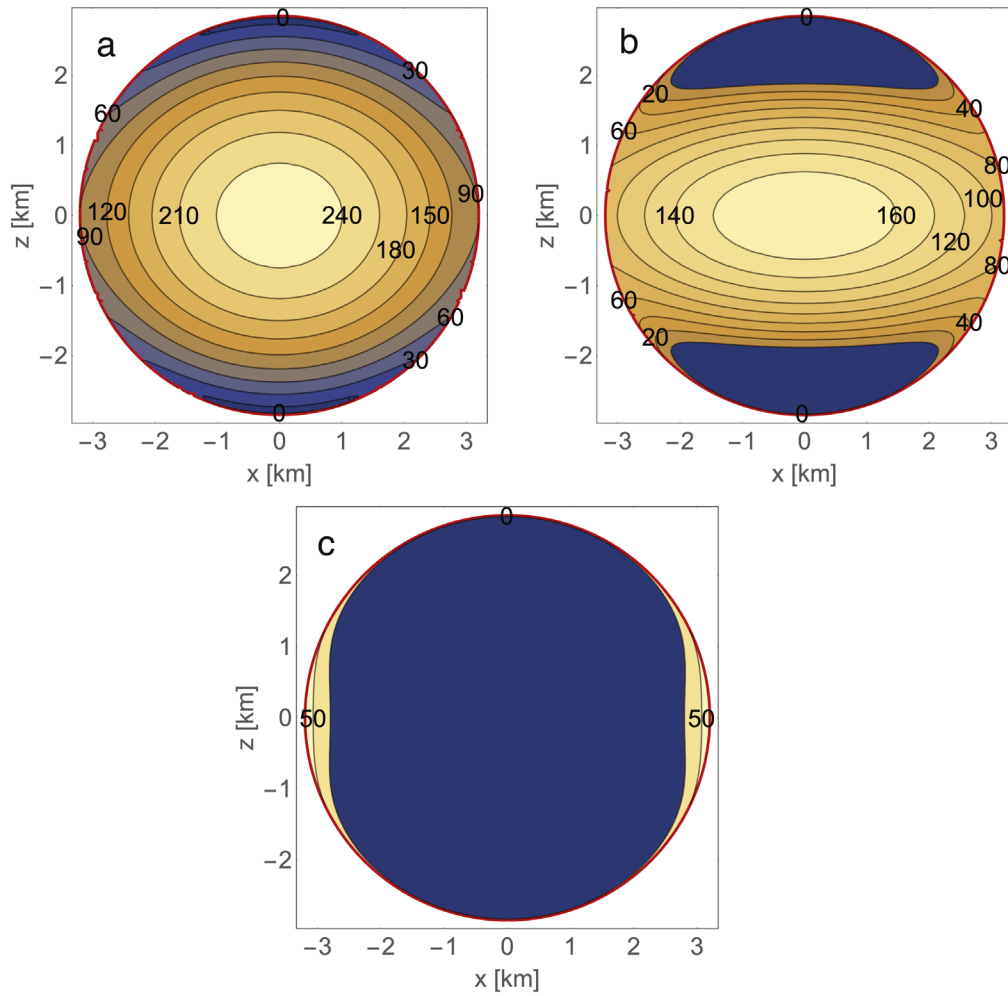
Figure 1. Distribution of Y^* at the x–z plane. The rotation period is 3.60 hr. Panels (a), (b), and (c) describe bulk densities of 0.5, 1.0, and 1.5 g cm^{-3}, respectively.
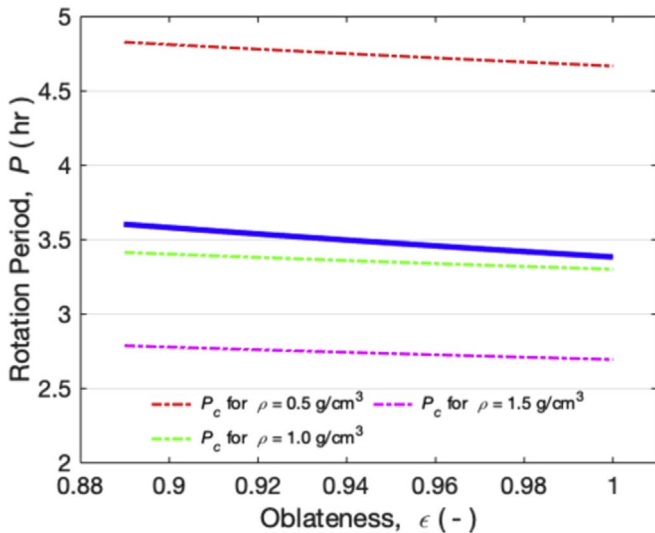

Figure 2. Rotation period as a function of the oblateness (the blue solid line). $P = 3.60$ hr when $\epsilon = 0.889$ and $P = 3.38$ hr when $\epsilon = 1.0$. The dotted lines indicate P_c for different bulk densities: the red, green, and magenta lines show bulk densities of 0.5, 1.0, and 1.5 g cm^{-3}, respectively.

Possible initiation processes such as thermal waves during Phaethon's apparition passages triggered reshaping, and rotational deformation enhanced this reshaping process

significantly. Because the rotation period at this stage was closer to or above P_c, the reshaping process caused mass shedding at large scale, which became a source of the Geminid meteor stream. Thus, the current oblate shape maybe a remnant of this large deformation event. When the oblateness evolved, the rotation of Phaethon slowed down. However, the structure was still sensitive to failure. When there is similar perturbation such as thermal waves at present, rotationally driven failure can be triggered; however, because the centrifugal effect is less significant, the magnitude of mass shedding is less intense than that in the past.

While we cannot strongly constrain whether the generation of the Geminid meteor stream was a single event or episodic, our study gives some hints of large-scaled mass-shedding processes as a source of the Geminid meteor stream. Because the generation of the Geminid meteor stream may have occurred within the last 1 ka (Gustafson 1989; Williams & Wu 1993; Ryabova 2007), the large-scaled reshaping and mass-shedding processes may have occurred in this timescale. These processes should be more rapid and intense to be completed (within the last 1 ka) than the Yarkovsky–O'Keefe–Radzievskii–Paddack (YORP) effect driven evolution, which may take ~1 Ma based on earlier work (Čapek & Vokrouhlický 2004; Bottke et al. 2006). Given this short timescale, a possible explanation of the deformation mode may
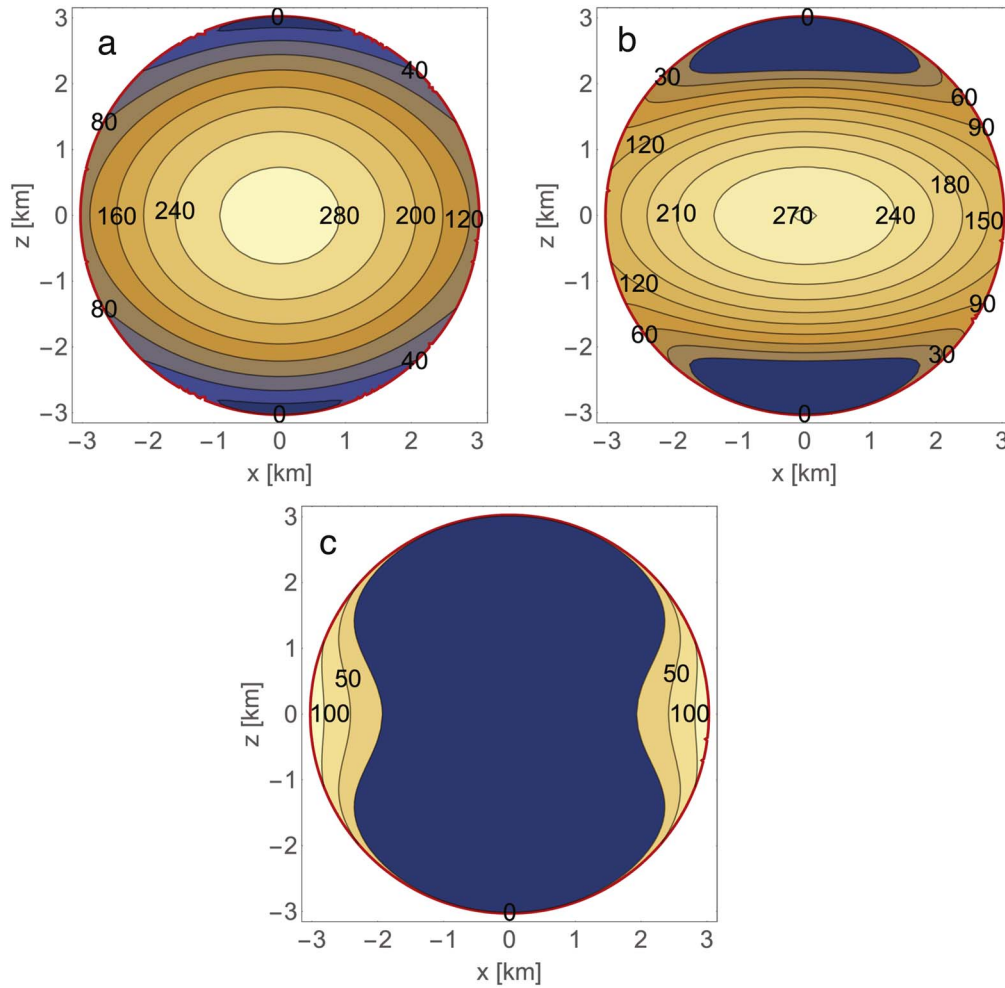
Figure 3. Distribution of Y^* at the x–z plane. The rotation period is 3.38 hr. Panels (a), (b), and (c) describe bulk densities of 0.5, 1.0, and 1.5 g cm^{-3}, respectively.

be internal failure, which can provide large-scaled deformation and thus mass shedding at fast rotation (Hirabayashi 2015).

We note that the total mass of the Geminid meteor stream is about 2.5% of that of Phaethon. If a mass shedding that can even produce the same magnitude of the Geminid meteor stream occurs every 1ka, the lifetime of Phaethon would only be ∼40 ka, which may be much shorter than that predicted by the orbital evolution, ∼26 Ma (De León et al. 2010). While there is no decisive evidence, the YORP effect may give some insights into this discrepancy. The YORP evolution timescale of Phaethon may become longer by many different factors such as the mass, shape, surface composition, and stochastic evolution (Bottke et al. 2015). Furthermore, its highly eccentric orbit, $e = 0.890$, with a small perihelion distance of 0.14 au (JPL Small-Body Database) may give strong variations in solar radiation acting on Phaethon. Thus, it may be possible that Phaethon has stochastically spun up by the YORP effect for the entire orbital age, ∼26 Ma (De León et al. 2010), and it recently experienced large-scaled mass shedding that formed the Geminid meteor stream. Then, a large mass-shedding event that produced the Geminid meteor stream may have decelerated Phaethon's spin, but the spin state after this event may have been still high enough to have some mass-shedding events at a small level, similar to what we observed in 2009 and 2012 (Jewitt & Li 2010; Jewitt 2012; Li & Jewitt 2013). To fully address the detailed timescale of the rotationally driven

reshaping process is beyond the scope of this study; we leave this problem as future work.

Finally, We assumed that Phaethon currently has a top shape having Bennus oblateness, $\epsilon = 0.889$, by following Taylor et al. (2019). To check if this setting is consistent with other top-shaped asteroids, we consider six top-shaped near-Earth asteroids: Ryugu (Watanabe et al. 2019), 1994 KW4 (Ostro et al. 2006), 2008 EV5 (Busch et al. 2011), 1994 CC (Brozović et al. 2011), 2001 SN 263 (Becker et al. 2015), and 2000 DP107 (Naidu et al. 2015). We find the range of ϵ to be 0.873–0.968, and thus Bennus ϵ is within this range. We conduct the same analyses for these objects and found trends similar to Bennus. The variation in the oblateness at this magnitude does not affect the results of Y^* significantly, which is less than 12%. Therefore, we conclude that our oblateness setting is meaningful to capture a possible scenario of Phaethon's activities.

Potential issues. We finally address issues of our analysis approach. This study explored Phaethon's rotationally induced structural failure by modeling Phaethon as a triaxial ellipsoid. We did not account for local topographic features; therefore, our semi-analytical model does not capture local deformations that may differ from global deformations (Hirabayashi & Scheeres 2019; Hirabayashi et al. 2019). However, Hirabayashi (2015), who compared an analytical solution and a finite element method (FEM) solution, found that there was no significant variation between the two. Therefore, we conclude
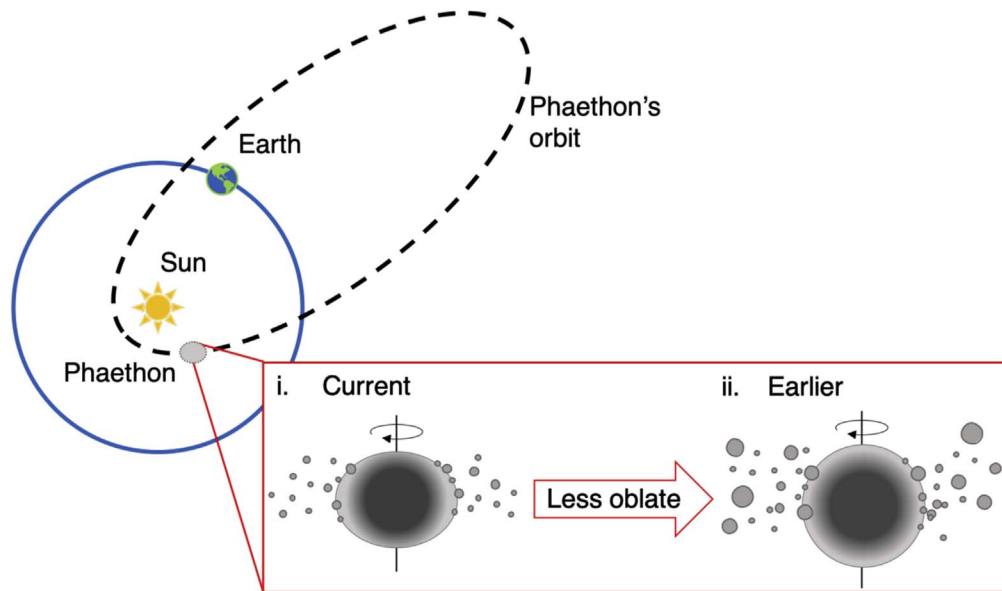
Figure 4. Possible evolution scenario of Phaethon. Phaethon has a highly eccentric orbit ($e = 0.890$) with a small perihelion distance of 0.14 au. At an earlier stage, Phaethon was less oblate and rotating faster, leading to mass shedding at a larger scale. For both stages, perturbation such as thermal waves may be a possible trigger for mass shedding.

that our semi-analytical model can provide solutions with reasonable accuracy. It is our future work to perform FEM analysis using a shape model to investigate the local deformations.

Another issue to be addressed is that our model does not assert the detailed failure mode. While numerous research studies have been undertaken, it is still not well determined how top-shape asteroids deform. Hirabayashi (2015) showed that depending on the internal structure and the bulk density, the failure mode may become different either in surface processing or internal deformation. However, because our semi-analytical model can only describe a homogeneous structure, we cannot infer how Phaethon's deformation is controlled by the heterogeneity. Therefore, the detailed failure mode cannot be specified. If Phaethon's heterogeneous structure is revealed, we need to employ a different approach (i.e., Hirabayashi et al. 2015).

There still remain many unknowns regarding Phaethon's physical properties. We will further elaborate our approach to give constraints on the activity of Phaethon. Concurrently, further constraints are vitally important to support DESTINY+.

ORCID iDs

Ryota Nakano ⓘ https://orcid.org/0000-0002-9840-2416
Masatoshi Hirabayashi ⓘ https://orcid.org/0000-0002-1821-5689

References

Arai, T., Kobayashi, M., Ishibashi, K., & Yoshida, F. 2018, LPI, 49, 2570
Barnouin, O. S., Daly, M. G., Palmer, E. E., et al. 2019, NatGe, 12, 247
Becker, T. M., Howell, E. S., Nolan, M. C., et al. 2015, Icar, 248, 499
Bottke, W. F., Vokrouhlický, D., Rubincam, D. P., & Nesvorný, D. 2006, AREPS, 34, 157
Bottke, W. F., Vokrouhlický, D., Walsh, K. J., et al. 2015, Icar, 247, 191
Brozović, M., Benner, L. A., Taylor, P. A., et al. 2011, Icar, 216, 241
Busch, M. W., Ostro, S. J., Benner, L. A., et al. 2011, Icar, 212, 649
Chamberlin, A. B., McFadden, L. A., Schulz, R., Schleicher, D. G., & Bus, S. J. 1996, Icar, 119, 173
Chen, W.-F., & Han, D.-J. 1988, Plasticity for Structural Engineers (Fort Lauderdale, FL: J. Ross Publishing, Inc.)
Cochran, A. L., & Barker, E. S. 1984, Icar, 59, 296
De León, J., Campins, H., Tsiganis, K., Morbidelli, A., & Licandro, J. 2010, A&A, 513, A26
Dobrovolskis, A. R. 1982, Icar, 52, 136
Gustafson, B. A. S. 1989, A&A, 225, 533
Hirabayashi, M. 2015, MNRAS, 454, 2249
Hirabayashi, M., Sánchez, D. P., & Scheeres, D. J. 2015, ApJ, 808, 63
Hirabayashi, M., & Scheeres, D. J. 2015, ApJL, 798, L8
Hirabayashi, M., & Scheeres, D. J. 2019, Icar, 317, 354
Hirabayashi, M., Tatsumi, E., Miyamoto, H., et al. 2019, ApJL, 874, L10
Holsapple, K. A. 2001, Icar, 154, 432
Hsieh, H. H., & Jewitt, D. 2005, ApJ, 624, 1093
Hughes, D. W., & McBride, N. 1989, MNRAS, 240, 73
Jenniskens, P. 1994, A&A, 287, 990
Jewitt, D., & Li, J. 2010, AJ, 140, 1519
Jewitt, D., Li, J., & Agarwal, J. 2013, ApJL, 771, 1
Jewitt, D. 2012, AJ, 143, 66
Kitazato, K., Milliken, R. E., Iwata, T., et al. 2019, Sci, 364, 272
Lambe, W., & Whitman, R. 1969, Soil Mechanics (New York: Wiley)
Lauretta, D. S., Hergenrother, C. W., Chesley, S. R., & Leonard, J. M. 2019, Sci, 366, 6470
Li, J., & Jewitt, D. 2013, AJ, 145, 154
Love, A. E. H. 2013, A Treatise on the Mathematical Theory of Elasticity (Cambridge: Cambridge Univ. Press)
Naidu, S. P., Margot, J. L., Taylor, P. A., et al. 2015, AJ, 150, 54
Ostro, S. J., Margot, J. L., Benner, L. A. M., Giorgini, J. D., & Scheeres, D. J. 2006, Natur, 314, 1276
Ryabova, G. O. 2007, MNRAS, 375, 1371
Scheeres, D. J., McMahon, J. W., French, A. S., et al. 2019, NatAs, 3, 352
Scheeres, D. J., & Sánchez, P. 2018, PEPS, 5, 25
Sugita, S., Honda, R., Morota, T., et al. 2019, Sci, 364, 252
Taylor, P. A., Rivera-Valentín, E. G., Benner, L. A., et al. 2019, P&SS, 167, 1
Čapek, D., & Vokrouhlický, D. 2004, Icar, 172, 526
Walsh, K. J., Richardson, D. C., & Michel, P. 2008, Natur, 454, 188
Walsh, K. J., Richardson, D. C., & Michel, P. 2012, Icar, 220, 514
Watanabe, S., Hirabayashi, M., Hirata, N., et al. 2019, Sci, 364, 268
Whipple, F. 1983, IAUC, 3881, 1
Wiegert, P. A., Houde, M., & Peng, R. 2008, Icar, 194, 843
Williams, I. P., & Wu, Z. 1993, MNRAS, 262, 231